ADVANCED FUNCTIONAL MATERIALS
www.afm-journal.de

Materials Views
www.MaterialsViews.com

In Situ Generated Gas Bubble-Directed Self-Assembly: Synthesis, and Peculiar Magnetic and Electrochemical Properties of Vertically Aligned Arrays of High-Density Co_3O_4 Nanotubes

Guoxiu Tong, Jianguo Guan, and Qingjie Zhang*

A novel and versatile gas bubble induced self-assembly technique is developed for the one-step fabrication of vertically aligned polycrystalline Co_3O_4 nanotube arrays (NTAs) by the rapid thermal decomposition of $Co(NO_3)_2{\cdot}6H_2O$ on a flat substrate. In this protocol, the in situ generation and release of gas bubbles, which can be regulated by elaborately adjusting the kinetic factors such as reaction time, decomposition temperature and pressure as well as the content of the chemically adsorbed water, play a vital role in the formation of the Co_3O_4 NTAs. Due to the shape anisotropy, ordered hierarchically porous structure and high surface area, the as-obtained Co_3O_4 NTAs show unique magnetic properties of a low Néel temperature and a large exchange bias field, as well as an initial discharge capacity up to 1293 $mAh{\cdot}g^{-1}$ at 35 $mA{\cdot}g^{-1}$ and the retention of a charge capacity as high as 895.4 $mAh{\cdot}g^{-1}$ after 10 cycles. This endows them with important potential use in magnetic shielding, magnetic recording media, and lithium ion batteries, etc. Due to the simplicity of the self-assembly method, this process is applicable to the large-scale production of the Co_3O_4 NTAs, and may be extended to other materials.

1. Introduction

Increasing attention has been paid to vertically aligned arrays of nanowires and nanotubes because they can serve as the building blocks for constructing optical, electronic, and electromechanical devices through the “bottom up” approach.[1] Much effort has been devoted to the fabrication of such arrays, with strategies including template-assisted synthesis,[2] solvothermal/hydrothermal process,[3] physical vapor deposition,[4] etc. However, most of these approaches require either porous templates or tedious procedures. In particular, when templates are used, post-synthesis removal of the templates may break the nanostructures and at the same time introduce unwanted defects or impurities. For these reasons, it remains a great challenge to develop a templateless, facile, and versatile procedure for fabricating nanotube arrays (NTAs).

As an important magnetic, *p*-type semiconductor, cobalt oxide (Co_3O_4) has many interesting applications, for example, in the fabrication of sensors, heterogeneous catalysts, electrochromic devices, Li-ion batteries, and rotatable magnets.[5–7] The synthesis of nanostructured Co_3O_4 has been widely explored, as they have high surface areas, peculiar chemical and physical properties, and thus improve the above applications. To date, simple Co_3O_4 nanostructures, such as spheres, flakes, rods, wires, and tubes,[6] as well as arrays of Co_3O_4 nanowires, nanorods, nanoneedles, and hollow-spheres[7] have been obtained. However, to the best of our knowledge, there are no reports concerning with complex nanostructures of Co_3O_4 nanotube arrays vertically standing on flat substrates. On the other hand, the gas bubble-assisted synthesis strategy has recently attracted much interest for its simplicity, high efficiency, and low cost.[8] In particular, it does not require templates and is able to tailor the morphology of the resultant nanostructures by kinetically controlling the number, distribution, size, and released rate of gas bubbles in the dispersion system.[9,10] So far, some particular structures including microcontainers (bowls, cups, goblets, and bottles),[11] microrings/microholes,[12] 3D structures,[13] hollow spheres,[14] and nanorods/nanocircles,[15] have been obtained using this approach.

In the present work, we develop a simple gas bubble-induced self-assembly technique for the one-step fabrication of vertically aligned arrays of Co_3O_4 nanotubes. In this approach, the rapid thermal decomposition of hydrous cobalt nitrate in situ generates numerous gas bubbles, which direct the formation of vertically aligned Co_3O_4 nanotube arrays on flat substrates by adjusting the kinetic factors such as decomposition temperature and pressure. The as-obtained Co_3O_4 NTAs are constructed by uniform nanotubes of about 300 nm in length and with one end freestanding and the other end merged into a film. In

Dr. G. X. Tong, Prof. J. G. Guan, Prof. Q. J. Zhang
State Key Laboratory of Advanced Technology
for Materials Synthesis and Processing
Wuhan University of Technology
No.122, Luoshi Road, Wuhan 430070, P. R. China
E-mail: guanjg@whut.edu.cn
Dr. G. X. Tong
College of Chemistry and Life Sciences
Zhejiang Normal University
Jinhua 321004, P. R. China

DOI: 10.1002/adfm.201202747

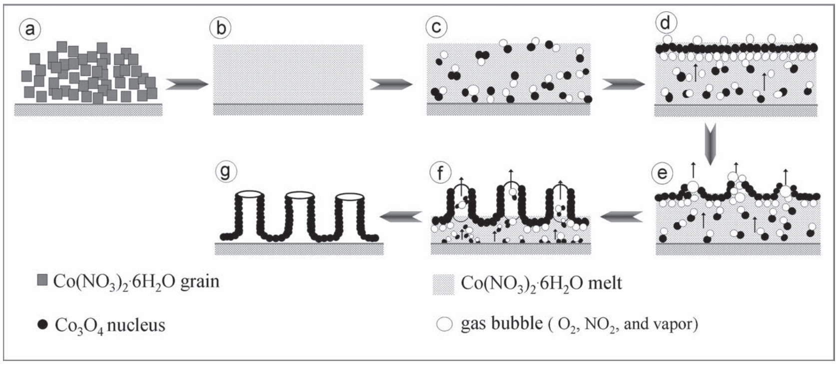

Scheme 1. A schematic illustration of the procedure for generating vertically aligned arrays of Co_3O_4 nanotubes.

combination with the unique formation process, the peculiar morphologies and structures including the shape and surface anisotropy, ordered porosity, and high surface area endow them with the great enhancement of magnetic properties and electrochemical activity. Due to the simplicity of this novel approach, it is applicable to the large-scale production of Co_3O_4 NTAs and other metal and/or metal oxide nanotubes or NTAs on substrates. Moreover, the novel Co_3O_4 NTAs obtained here can be expected to have promising applications in magnetic recording media, magnetic shielding, lithium-ion batteries, chemical sensing, etc.

2. Results and Discussion

2.1. Structure Characterization and Formation Mechanism

The vertically aligned arrays of Co_3O_4 nanotubes were synthesized by uniformly spreading $Co(NO_3)_2{\cdot}6H_2O$ solid powders on a planar stainless steel substrate and heating at 300 °C for about 10 min, during which the pink powders were firstly melted, then turned into a black film covering the substrate. **Scheme 1** shows a schematic illustration of the procedure we used for generating the vertically aligned arrays of Co_3O_4 nanotubes. Four major steps are involved: 1) $Co(NO_3)_2{\cdot}6H_2O$ grains (a) quickly melt into a thin liquid membrane (b), which covers the substrate, as it has a melting point of only 55 °C; 2) thermal decomposition of $Co(NO_3)_2{\cdot}6H_2O$, which is characterized by TG-DSC (see Supporting Information Figure S1), occurs in the term of the following chemical reactions:[16,17]

$$\begin{aligned} &Co(NO_3)_2\cdot 6H_2O \xrightarrow{-3H_2O} Co(NO_3)_2 \\ &\cdot 3H_2O \xrightarrow{-HNO_3} Co_2(NO_3)_3(OH)\cdot 5H_2O \end{aligned} \tag{1}$$

$$\begin{aligned} &Co_2(NO_3)_3(OH) \\ &\cdot 5H_2O \xrightarrow{-HNO_3} Co_2(NO_3)_2(OH)_2\cdot 4H_2O \end{aligned} \tag{2}$$

$$\begin{aligned} &Co_2(NO_3)_2(OH)_2 \\ &\cdot 4H_2O \xrightarrow{-NO_2-5H_2O} CoOCoONO_3 \xrightarrow{-3NO_2+\frac{1}{2}O_2} 2Co_3O_4 \end{aligned} \tag{3}$$

$$12HNO_3 \longrightarrow 4NO_2 + 4N_2O + 9O_2 + 6H_2O \tag{4}$$

Obviously, the products are Co_3O_4 nuclei in combination with a large amount of gas bubbles including O_2, NO_2, and water vapor (c), which take the Co_3O_4 nuclei to the solution surface to form a Co_3O_4 thin film (d); 3) freshly generated gas bubbles break through the Co_3O_4 thin film due to the increasing pressure, forming protrusion crevasses or holes (e); 4) nanotubes grow at the edge of the holes via the mass transportation of continually generated Co_3O_4 nuclei induced by the in situ generated gas bubbles (f), resulting in the formation of vertically aligned arrays of Co_3O_4 nanotubes (g).

Figure 1 shows scanning electron microscopy (SEM) and transmission electron microscopy (TEM) characterization of the as-prepared arrays of Co_3O_4 nanotubes. Clearly, the black film is made of a vertically aligned array of nanotubes with an open end (Figure 1a). The nanotubes were 50–60 nm in outer diameter, with a wall thickness of 10 nm. The nanotubes showed a relatively rough surface feature (inset of Figure 1a). All nanotubes have a relatively uniform length up to about 300 nm, with one end freestanding and the other end merged into a film (Figure 1b). The back surface of the film consists of regularly alternating concavo-convex boundaries, implying that all the distance between nanotubes are about 100 nm and the holes seen in the top view continually extend into the backside of the film. The TEM images (Figures 1c,d) also substantiate this. The bended nanotube shown in Figure 1d is found in the same sample, suggesting good flexibility for these nanotubes. The existence of randomly oriented lattice stripes in Figure 1e suggests a polycrystalline structure. This is further confirmed by the SAED pattern. The lattice fringe of about 0.46 nm is in accord with the separation between the (111) planes of Co_3O_4. Weak diffraction rings in Figure 1f are indexed to the peaks from Co_3O_4. Meanwhile, the presence of vast micropores implies that the arrayed nanotubes should have a high surface area. Also, the other information from energy dispersive X-ray spectroscopy (EDX), X-ray diffraction (XRD), infrared (IR) and Raman spectra (see Supporting Information Figure S2,S3), as well as the X-ray photoelectron spectroscopy (XPS) (see Supporting Information Figure S4), reconfirms the presence of face-centered cubic Co_3O_4 with spinel structure. In addition, the Brunauer–Emmett–Teller (BET) specific surface area and the pore size distribution curves corresponding to the aforementioned Co_3O_4 NTAs show the bimodal pore-size distribution with the BET surface area of 41.07 $m^2{\cdot}g^{-1}$ (see Supporting Information Figure S5).

There is so far a great challenge in modulation over the production of gas bubbles in a quantificational and precise manner for materials scientists and chemists since it is too complicated to accurately determine the size and number of the gas nano-/microbubbles. To decipher the in situ generated gas bubble-induced self-assembly mechanism, we systematically investigated the effects of the reaction conditions on the dimension and morphology of the resultant products. For example, we used SEM to check the morphological evolution of the intermediate products obtained at different stages of a typical synthesis. As the decomposition reaction started, we observed at

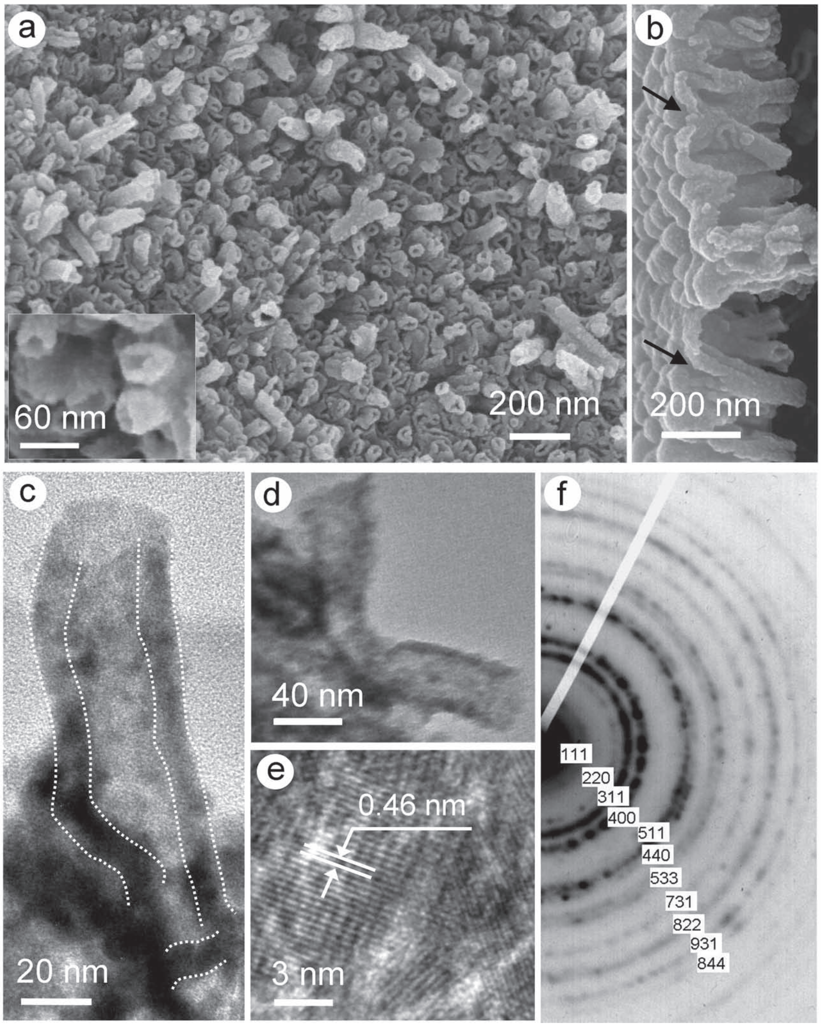

Figure 1. a) Top view and b) tilted side view of the arrayed Co_3O_4 nanotubes formed via thermal decomposition of $Co(NO_3)_2{\cdot}6H_2O$ on Fe foil at 300 °C. The inset of (a) shows a high-magnification field emission scanning electron microscopy (FESEM) image of the top end. c,d) TEM and e) high-resolution TEM images of single Co_3O_4 nanotubes detached from the array, and f) the corresponding selected area electron diffraction (SAED) pattern. The dotted lines are added as a guide to discern the wall-thickness of the nanotubes.

the reaction time (*t*) of 0.5 min a thin film consisting of nanoparticles (**Figure 2**a), which then evolved into protrusion apexes at $t = 1$ min (Figure 2b), followed by the formation and growth of sparse short Co_3O_4 nanotubes at $t = 5$ min (Figure 2c). Further prolonging *t* to 10 min, the Co_3O_4 NTAs with more uniform, longer, and denser nanotubes formed (Figure 2d). This can be explained by the fact that the longer the length of the Co_3O_4 nanotube is, the larger the resistance of the nanotube wall to gas-bubbles is. As a result, new protrusion apexes and nanotubes produced in the blank spaces, which made the NTAs more uniform and denser. Obviously, the aforesaid morphological evolution agrees with our proposed mechanism of the gas-bubbles induced self-assembly, as illustrated in Scheme 1. In fact, the *t* dependence of product morphology provides us important guidance that changing *t* could effectively adjust the length and density of the nanotubes.

From **Figure 3**, we can clearly observe that changing the decomposition temperature (*T*) produces various nanostructures. In our protocol, *T* affects in two aspects on the formation of Co_3O_4 nanostructures. One is to provide a driving force for the decomposition of $Co(NO_3)_2{\cdot}6H_2O$ together with the nucleation and growth of Co_3O_4. The other is to modulate the viscosity of molten $Co(NO_3)_2{\cdot}6H_2O$[18] and the diffusion/assembly behavior of the gas-bubbles. All of these details play critical roles in the formation of the Co_3O_4 NTAs. For example, no NTAs but contorted, tube-like Co_3O_4 nanostructures were found at lower *T* of ca. 200 °C. A possible reason is that lower temperature greatly slows down the decomposition reaction rate and augments the viscosity of molten $Co(NO_3)_2{\cdot}6H_2O$, which facilitates the formation of intermittent column-like gas-flows, causing the formation of contorted, tube-like Co_3O_4 nanostructures (Figure 3a,b). However, at the relatively high *T* (e.g. 450 °C), only mesoporous rod-like structures composed by a mass of nanoparticles, with a relatively rough surface, were obtained (Figure 3c). Further increasing *T* to 500 °C produced only solid nanorods with relatively smooth surfaces (Figure 3d). It is conceivable that the low viscosity and high reaction rate of molten $Co(NO_3)_2{\cdot}6H_2O$ at the relatively high *T* increase the diffusion/aggregation rate of the gas bubbles, which favors the assembly of Co_3O_4 nuclei. However, the relatively high *T* also provides a powerful driving force for the growth of the nanocrystals, which grow up by the mergence of Co_3O_4 nuclei or nanoparticles. This results in the shrinkage and even disappearance of the pores with increasing *T*. The above results indicate that changing *T* can effectively tailor the inner diameter of the as-made nanotubes.

Also, to investigate the role of water vapor in the formation of the NTAs, we first vaporized the partial crystallization water by heating $Co(NO_3)_2{\cdot}6H_2O$ at 90 °C for 5 h, and then gain the Co_3O_4 products via decomposing the remainder at 300 °C for 10 min. As shown in **Figure 4**a, only the porous film consisting of the nanoparticles is formed. This implies that crystallization water plays a key role in the formation of the NTAs. The existence of crystallization water provides a fluid phase environment for the transportation of the gas bubbles and Co_3O_4 nucleus, and adjusts the viscosity of the fluid phase. On the other hand, crystallization water produces a mass of gas bubbles, which act as the template for the assembly of the Co_3O_4 nuclei.

Figure 4b shows that only a mass of fragmented flakes are obtained if the decomposition of $Co(NO_3)_2{\cdot}6H_2O$ powders is carried out under vacuum at 300 °C, while Figure 4c shows that Co_3O_4 octahedra are formed under high pressure decomposition of $Co(NO_3)_2{\cdot}6H_2O$ powders. This is because

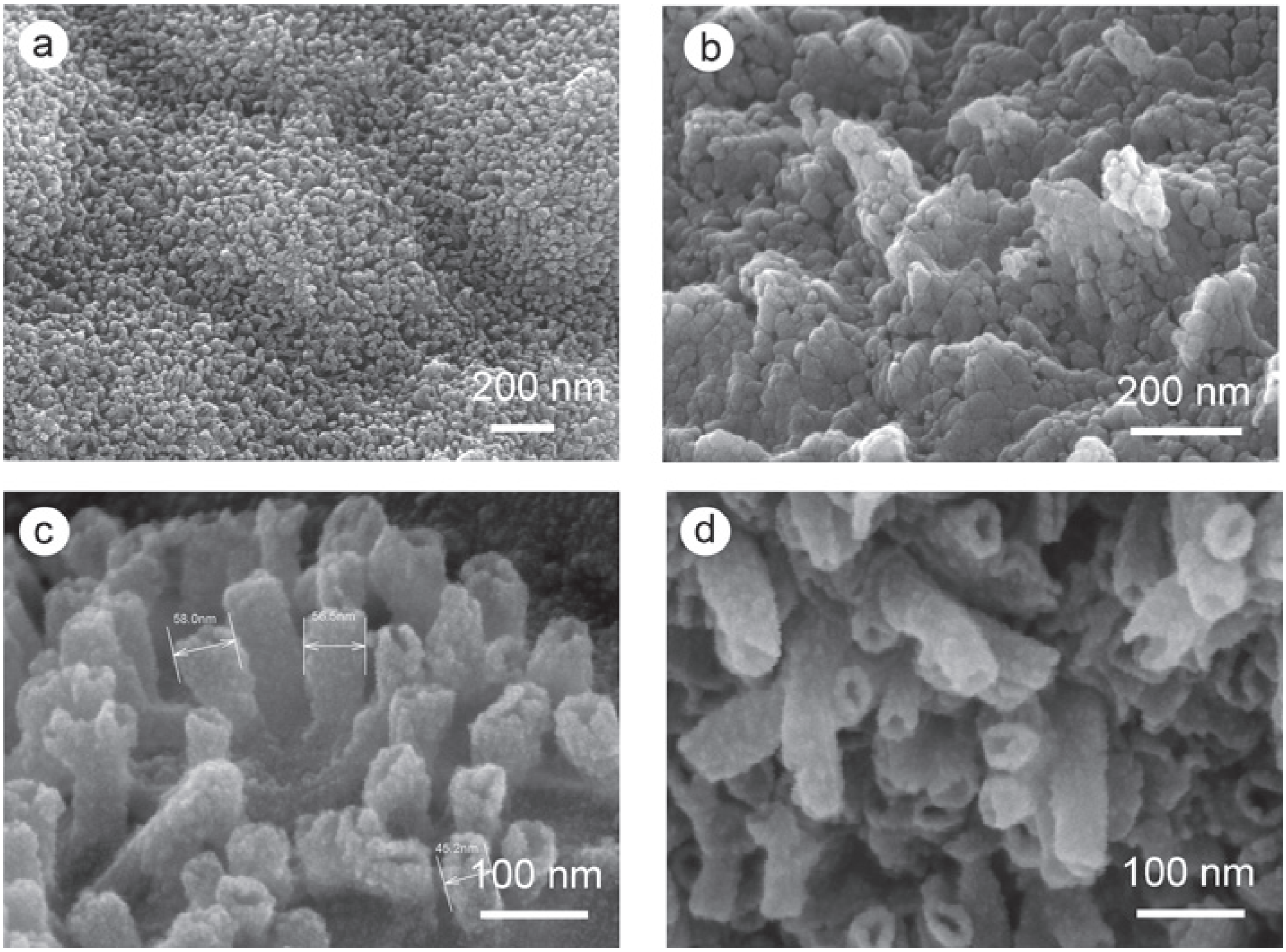

Figure 2. FESEM images of the intermediate products obtained at different reaction time of a) 0.5 min, b) 1 min, c) 5 min, and d) 10 min, respectively. The nanograin film, protrusion crevasses, short NTAs and NTAs occurred successively as the decomposition continued at 300 °C.

the air pressure determines not only the adsorption/desorption behavior of the in situ generated gas bubbles on the nucleus surfaces but also the growth rate of Co_3O_4 nuclei. Generally, low pressure in the reaction system causes gas bubbles generated in situ from the nucleus surfaces to quickly desorb, which destroys the self-assembly behavior of nanocrystals.[9c] On the contrary, relatively high pressure in the reaction system hinders the formation and transportation of gas bubbles, and is helpful for the growth of Co_3O_4 nuclei, leading to the formation of Co_3O_4 octahedra (Figure 4c).

Clearly, the above experimental observations are in good agreement with our proposed mechanism illustrated in Scheme 1. It is reasonable to conclude that the viscosity of the carrier solution, the number, size and transport rate of the gas bubbles, and the growth rate of the Co_3O_4 nucleus all strongly influence the gas-bubble-induced assembly of Co_3O_4 nucleus into NTAs,[9a,c] and they can be tuned by changing the reaction time, temperature, and even air pressure. The length and inner diameter of the nanotubes can be adjusted by modulating the reaction time and temperature, respectively. A systematic study is under way to control the length and wall thickness of the arrayed nanotubes on a large scale.

2.2. Magnetic Properties

Figure 5a shows the zero-field cooled (ZFC) and the field cooled (FC) magnetization curves of the Co_3O_4 NTAs obtained at 300 °C with an applied field of 100 Oe. With increasing temperature from 3.5 K to 270 K, both of them first sharply decrease up to 25 K, and then slowly decrease. This suggests that the Co_3O_4 NTAs have a phase transition temperature at 25 K (Néel temperature, T_N), which is close to that of Co_3O_4 nanoparticles,[19] lower than that for Co_3O_4 nanoflowers (33 K)[20] and that for the bulk Co_3O_4 (40 K).[21] The lower T_N can be attributed to the finite size and surface effect, as T_N of the nanomaterials decreases with the decrease of crystal size.[22]

Figure 5b further reveals that the magnetization (M) of the products at $T \geq 25$ K obeys the Curie–Weiss law with a negative θ_p value of about −138 K. The effective magnetic moment per ion (μ_{eff}) in the paramagnetic state for Co_3O_4 NTAs can be estimated to be about $4.4\mu_B$. At $T \leq 25$ K, the reciprocal susceptibility (χ^{-1}) versus temperature shows a nonlinear plot. This is ascribed to the coexistence of the spontaneous magnetization and the immanent magnetic moment. In general, bulk Co_3O_4 with a normal spinel structure, which contains 16 octahedral

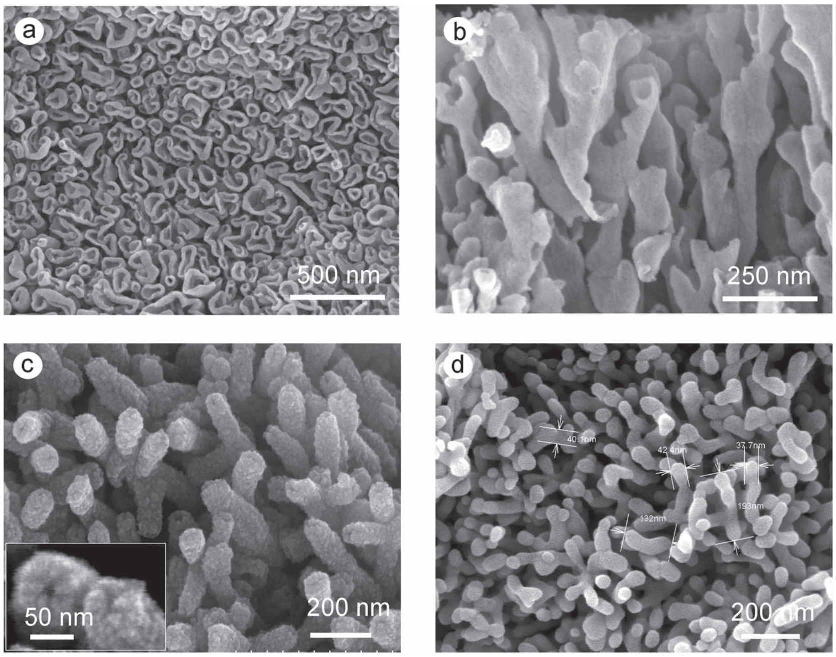

Figure 3. FESEM images of the Co_3O_4 nanostructures formed via thermal decomposition of $Co(NO_3)_2{\cdot}6H_2O$ on Fe foil at different temperatures of (a: top view, b: front view) 200 °C; (c: tilted top view) 450 °C and (d: tilted top view) 500 °C for 10 min. The inset in (c) shows a high-magnification FESEM image of the top end.

Co^{3+} ions of diamagnetism and 8 tetrahedral Co^{2+} ions of antiferromagnetism,[21] has an antiferromagnetic state owing to the spontaneous magnetization.[23] However, for the as-prepared Co_3O_4 NTAs, there exists a mass of surface and/or structure defects. These will cause the appearance of uncompensated surface spins in two sublattices[24] and/or multisublattice,[25] and induce the permanent magnetic moments of the antiferromagnetic superfine particles. The similar phenomenon is also found in the Co_3O_4 nanowire, nanotube and nanoparticles.[26] This suggests that the small size, large specific surface area, and hierarchically porous structures of the Co_3O_4 NTAs play significant roles in the weak ferromagnetic properties.

To further probe the magnetic property, the samples were cooled from 300 K to 3 K under a 100 Oe applied field (H_{FC}). Figure 5c shows the *M*–*H* loops at different temperatures in the 20 to −20 kOe ranges with the field direction parallel to H_{FC}. As shown in Figure 5d, the *M*–*H* loop at 10 K is unsymmetrical in shape around the origin, and shifts toward H_{FC}. This suggests the existence of unidirectional anisotropy and exchange bias field (H_e). As the measured temperature increases from 10 to 30 K, H_e decreases from 145 Oe to 3.02 Oe and hysteresis loops gradually narrow, indicating a decreasing coercivity (H_c). Further increasing the temperature from 30 to 300 K, H_e disappears and hysteresis loops become symmetric about the origin. This can be explained well in terms of the exchange coupling between ferromagnets (FM) and anti-ferromagnets (AFM). Generally, when a system consisting of FM and AFM is cooled lower than the T_N of the AFM, the exchange coupling between the FM and the AFM will induce a unidirectional anisotropy of the ferromagnetic layer. In this case, the hysteresis loop shifts horizontally.[27] Above T_N, the AFM spins are in a paramagnetic state, and thus can neither bias the ferromagnetic spins nor give rise to coercivity. This is consistent with Figure 5b. H_e for the as-obtained Co_3O_4 NTAs at 10 K (145 Oe) is significantly higher than that of nanoparticles at 5 K (110 Oe)[22b] and that of nanotubes at 1.8 K (98 Oe).[28] This is associated with the unique internal stress produced in the formation process as well as the peculiar shape and surface anisotropy[29] of the vertically aligned array of Co_3O_4 nanotubes, as shown in Figure 1. The similar phenomenon has been reported for Co_3O_4 mesoporous nanowires, which H_e varies with the order degrees of mesopores.[27] The H_e and related effects shown in the as-prepared Co_3O_4 NTAs imply that they may have several potential applications including permanent magnets, magnetic recording media or domain stabilizers in recording heads based on anisotropic magnetoresistance.

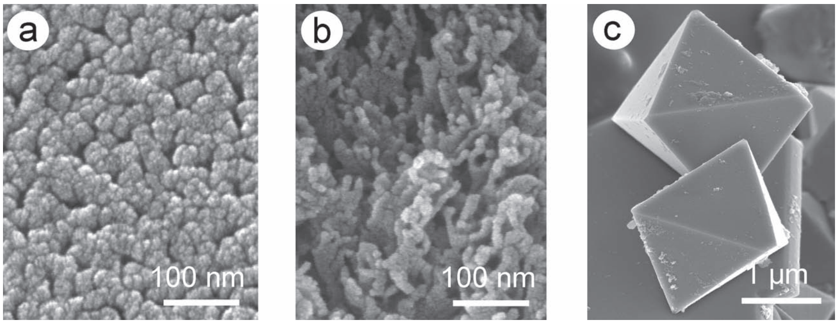

Figure 4. SEM images of various Co_3O_4 nanostructures formed via thermal decomposition of $Co(NO_3)_2{\cdot}6H_2O$ on Fe foil at a) 90 °C for 5 h then 300 °C for 10 min in an open system; b) 300 °C for 5 h in vacuum; and c) 300 °C for 5 h in a sealed Teflon autoclave.

2.3. Electrochemical Properties

The electrochemical performance of the as-prepared Co_3O_4 NTAs is evaluated by a standard method based on Co_3O_4/Li half cell, in which the Co_3O_4 NTAs and lithium foil act as a positive electrode and a negative electrode, respectively. **Figure 6**a shows the discharge–charge curves for the Co_3O_4 NTAs/Li half cell in the voltage window of 0.01–3 V at a current density (*J*) of 35 $mA{\cdot}g^{-1}$ and 20 °C. Obviously, during the first discharge the potential steeply falls to a small plateau at about 1.15 V, and then slowly drops to a large plateau at ca. 1.0 V until a capacity of 950 $mAh{\cdot}g^{-1}$, followed by a gradual decline in voltage till the end of discharge. In the subsequent cycles, there is only a discharge plateau at about 1.25 V and the charge plateau at about 1.9 V. The voltage versus capacity profile is similar to those of

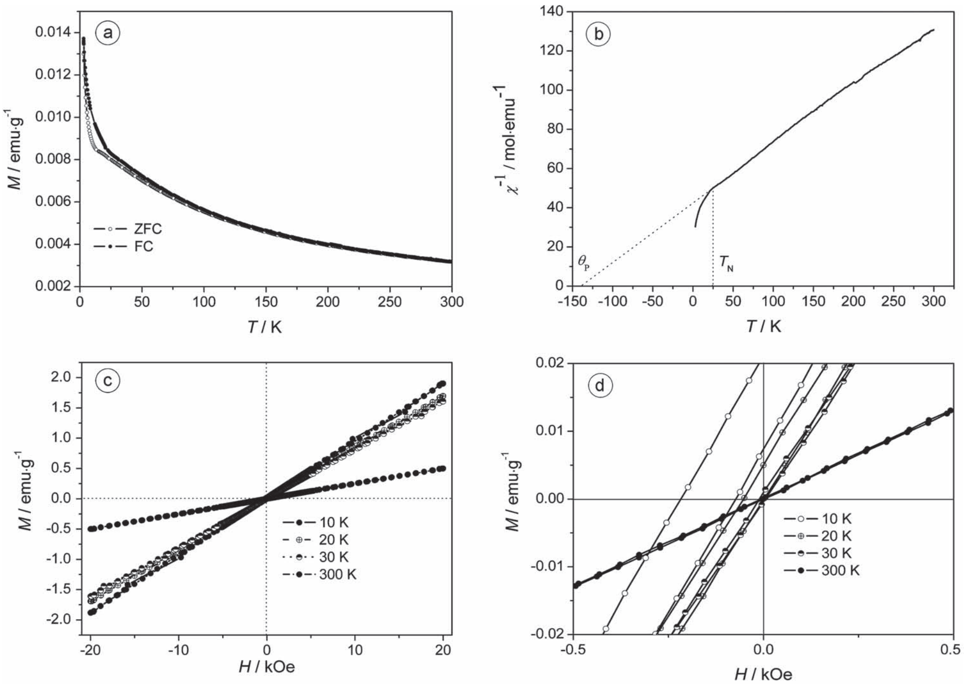

Figure 5. a) ZFC-FC Magnetization and b) χ^{-1} as a function of temperature (*T*) for the as-obtained Co_3O_4 NTAs under an applied field (*H*) of 100 Oe. c) Magnetization as a function of *H* for the as-obtained Co_3O_4 NTAs at the indicated temperatures. d) The enlarged central portion of the hysteresis loops in (c).

other Co_3O_4 nanomaterials.[30] According to the reaction mechanism proposed in the earlier studies,[5a,b,31] the electrochemical reaction of Li with Co_3O_4 involves the electrochemically driven formation of highly reactive metallic Co nanograins during the first discharge, accompanying the resultant formation-decomposition of amorphous Li_2O upon subsequent cycles, which differs from the classical Li insertion/deinsertion or Li alloying process. The detailed electrochemical reaction as follows:[32]

$$Co_3O_4 + 8Li \underset{charge}{\overset{discharge}{\rightleftarrows}} 4Li_2O + 3Co^0 \tag{5}$$

The multistep phase transformation of Co^{m+}/Co^0 (m = 2, 3) for Co^{3+} and Co^{2+} in Co_3O_4 corresponds to the different voltage plateaus. In the first discharge, a small voltage plateau at about 1.15 V versus Li^+/Li^0 for 1.1 Li^+ uptake corresponds to the reduction processes from Co^{3+} to Co^{2+}, whereas a distinct plateau at 1.0 V with 5.8 Li^+ uptake, followed by a gradual slope equivalent to another 4.4 Li^+ uptake, stands for the reduction processes from Co^{3+} to Co^{2+} and from Co^{2+} ion to Co^0. A similar result was observed in previous reports.[5a,7b]

Figure 6b shows the discharge and charge capacity versus cycle number for the Co_3O_4 NTAs electrodes at various *J*. The as-made Co_3O_4 NTAs show an initial discharge capacity as high as 1293 $mAh\cdot g^{-1}$ at 35 $mA\cdot g^{-1}$ and 1259.9 $mAh\cdot g^{-1}$ at 70 $mA\cdot g^{-1}$. These two values are higher than that of Co_3O_4 nanoparticles by ball-milling the decomposition product of $Co(NO_3)_2\cdot 6H_2O$ (830 $mAh\cdot g^{-1}$), that of Co_3O_4 nanorods obtained by calcining the precursor powder (815 $mAh\cdot g^{-1}$), that of Co_3O_4 nanotubes synthesized by a AAO template method (850 $mAh\cdot g^{-1}$),[5b] and that of mesoporous nanowire arrays (1124 $mAh\cdot g^{-1}$).[7b] Meanwhile, just as most anode materials,[5a,33–35] there is inevitably a large irreversible loss of 26–30% for the as-prepared Co_3O_4 NTAs in the first cycle. They still show a charge capacity as high as 955.2 $mAh\cdot g^{-1}$ at 35 $mA\cdot g^{-1}$ and 885.9 $mAh\cdot g^{-1}$ at 70 $mA\cdot g^{-1}$ after the first cycle, respectively. Moreover, this high value of 895.4 $mAh\cdot g^{-1}$ is almost completely retained even after 10 cycles. In contrast, the Co_3O_4 nanorods (NRs) obtained at 500 °C (Figure 3d) and spherical particles (Ps) at 700 °C (see Supporting Information Figure S6) only show a charge capacity of 709.8 $mAh\cdot g^{-1}$ at $J = 35$ $mA\cdot g^{-1}$ and 538.2 $mAh\cdot g^{-1}$ at $J = 35$ $mA\cdot g^{-1}$ after 10 cycles (Figure 6c), respectively.

In addition, the high value of 895.4 $mAh\cdot g^{-1}$ is almost equal to the theoretical capacity of Co_3O_4,[32,36] and obviously higher than that (750 $mAh\cdot g^{-1}$) of nanowires synthesized by virus template, and that (ca. 800 $mAh\cdot g^{-1}$) of mesoporous nanowire arrays.[7b] This indicates that the morphology and microstructure of nanostructured Co_3O_4 plays a significant role in determining the discharge–charge characteristics including the charge capacity. The superior electrochemical performance of the Co_3O_4 NTAs is associated with the hollow tubular structures, high specific surface areas and ordered arrangements, which favors the transport of lithium ions from both outer and inner part of the tube and makes the electrochemical reaction more active.

This suggests that the Co_3O_4 NTAs reported here are promising as a new class of negative electrode materials for lithium ion batteries because of their high capacity, though they also suffer from a poor capacity retention upon cycling and/or poor rate capability as in most of the present practical cells. Anyway, the nearly 100% capacity retention may come true by using additive or prelithiation for compensation, or the active modification of the tubular wall.[35,37]

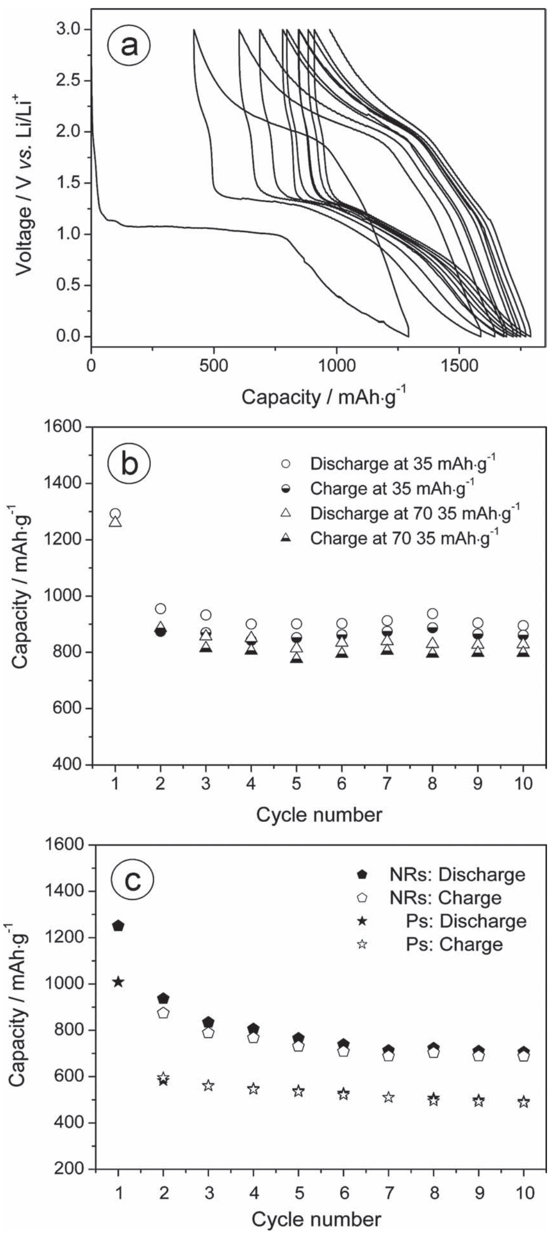

Figure 6. a) Discharge–charge curves of the electrodes made by the as-prepared Co_3O_4 NTAs obtained at 300 °C cycled between 3 and 0.01 V at the current density (J) of 35 mA·g^{-1} and 20 °C. Specific capacities versus cycle number for the electrodes made by Co_3O_4. b) NTAs at different J and c) nanorods (NRs) and particles (Ps) at J = 35 mA·g^{-1}.

3. Conclusions

In summary, we have demonstrated a versatile method based on thermal decomposition for preparing vertically aligned arrays of polycrystalline Co_3O_4 nanotubes, where the numerous gas bubbles generated in situ from the rapid thermal decomposition of hydrous cobalt nitrate direct the formation of vertically aligned Co_3O_4 nanotube arrays on flat substrates. The as-obtained vertically aligned arrays of polycrystalline Co_3O_4 nanotubes have hierarchically porous nanostructures, small size, and large specific surface area, and thus show unique weak ferromagnetic properties and superior electrochemical properties. Due to the simplicity of the preparation method, we believe that it should be applicable to the large-scale production of the Co_3O_4 nanotube arrays, and be extendable to other metal or metal oxide materials. Because of the high specific surface areas, unique magnetic properties, enhanced electrochemical activity, and the possibility to integrate with various substrates, these vertically aligned nanotubes are expected to find use in applications such as chemical sensing, magnetic shielding, field-emission, luminescence, and energy storage, etc.

4. Experimental Section

Preparation of Co_3O_4 Nanotube Array Films: All reagents, including cobalt nitrate hexahydrate ($Co(NO_3)_2{\cdot}6H_2O$, AR) were obtained from Shanghai Hengxin Chemical Reagent Co. Ltd. in China and were used without any further purification. In a typical synthesis, a stainless steel substrate with 4.0 cm × 4.0 cm × 3.0 mm in size was placed on a flat-heater (IKA C-MAG HS7) and was heated to 300 °C. Then, $Co(NO_3)_2{\cdot}6H_2O$ solid powders (2.97 g) were uniformly spread onto the substrate at once and kept at 300 °C for 10 min. A black film, which was easily peeled out of the substrate, was obtained by naturally cooling to room temperature with the flat-heater, washing with dieonized water and absolute ethanol for several times to remove unexpected impurities, and finally drying in a vacuum oven at 90 °C for 12 h. The reaction process was carried out within a mantle with an outlet to let the generated gases out to a sodium hydroxide solution (1.0 M) through a rubber pipe.

Characterization: The morphologies, chemical composition and crystalline structure of the as-prepared samples were studied by field-emission scanning electron microscope (FESEM, Hitachi S-4800, 10 kV), energy dispersive X-ray spectroscopy (EDX, Horbia EX-250, 20 kV) associated with FE-SEM, and high-resolution transmission electron microscopy (HRTEM, JEM-2100F, 200 kV), X-ray diffraction (XRD, D/MAX-IIIA, CuKα radiation, λ = 0.15406 nm, 10°/min), Fourier-transforming infrared (FTIR, Nicolet FTIR-170SX, 4000–400 cm^{-1}, room temperature) absorption spectra, micro-Raman spectroscopy (ISA T64000 triple grating system, Ar laser, λ = 514.5 nm), and X-ray photoelectron spectroscopy (XPS, XSAM800, Kratos Ltd., 2 × 10^{-7} Pa, 0.9 eV/10^4 CPS).

Differential scanning analysis/thermogravimetric analysis (DSC-TG) was carried out on a Netzsch STA 449C thermal analyzer. Nitrogen adsorption–desorption isotherms were obtained on a nitrogen adsorption apparatus (ASAP 2020M Micromeritics instruments, USA). The samples are degassed at 150 °C prior to Brunauer–Emmett–Teller (BET) measurements. The BET specific surface area (S_{BET}) is determined by a multipoint BET method using the adsorption data in the relative pressure P/P_0 range of 0.05–0.25. The pore size distribution was derived from the desorption isotherm using the Barret–Joyner–Halender method. The nitrogen adsorption volume at a P/P_0 of 0.995 was used to determine the pore volume and porosity.

Measurement of Properties: The magnetic properties for the samples in a powder form were carried out using a Model 4HF vibrating sample magnetometer (VSM, ADE, USA). Electrochemical measurements were carried out using two-electrode cells with lithium metals as the counter and reference electrodes. The working electrode was fabricated by compressing a mixture of the active materials including Co_3O_4 NTAs or nanoparticles, conductive material (acetylene black), and binder (polytetrafluoroethylene) in a weight ratio of 70:30:10. The electrode was dried at 80 °C for 1 h and cut into a disk of 1.0 cm in diameter. The battery assembly was performed in a glove-box filled with pure argon, in which the film negative piece, Celgard 2400 membrane, and lithium chip were sandwiched, and an appropriate amount of electrolyte was added before sealing. The newly installed battery was measured by a discharge-charge method in a multichannel battery tester (model Land CT2001A) in the potential range of 0–3.0 V after hold for 4 h.

Supporting Information

Supporting Information is available from the Wiley Online Library or from the author.

Acknowledgements

This work was supported by the National Natural Scientific Foundation of China (51002111 and 51102215), the Natural Science Foundation of Hubei Province (2010CDA030 and 2010CDB00606) and Zhejiang Province (Y4100022), the Subject Leadership Project of Wuhan City (201150530145), the Key Innovative Team of Magnetic Materials in Zhejiang Province (2011R09006-06), and the Science and Technology Projects from Jinhua City (2010A12066).

Received: September 21, 2012
Revised: November 8, 2012

---

[1] a) X. Wang, J. Song, J. Liu, Z. L. Wang, *Science* **2007**, *316*, 102; b) S. Da Col, M. Darques, O. Fruchart, L. Cagnon, *Appl. Phys. Lett.* **2011**,*98*, 112501; c) Y. Y. Song, Z. D. Gao, J. H. Wang, X. H. Xia, R. Lynch, *Adv. Funct. Mater.* **2011**, *21*, 1941; d) X. J. Feng, J. D. Sloppy, T. J. LaTempa, M. Paulose, S. Komarneni, N. Z. Bao, C. A. Grimes, *J. Mater. Chem.* **2011**, *21*, 13429; e) O. Assad, A. M. Leshansky, B. Wang, T. Stelzner, S. Christiansen, H. Haick, *ACS Nano* **2012**, *6*, 4702; f) C. N. R. Rao, A Govindaraj, *Adv. Mater.* **2009**, *21*, 4208; g) Y. Q. Dai, W. Y. Liu, E. Formo, Y. M. Sun, Y. N. Xia, *Polym. Adv. Technol.* **2011**, *22*, 326.

[2] a) H. Hillebrenner, F. Buyukserin, M. Kang, M. O. Mota, J. D. Stewart, C. R. Martin, *J. Am. Chem. Soc.* **2006**, *128*, 4236; b) F. W. Zhuge, J. J. Qiu, X. M. Li, X. D. Gao, X. Y. Gan, W. D. Yu, *Adv. Mater.* **2011**, *23*, 1330; c) J. Z. Wang, N. Du, H. Zhang, J. X. Yu, D. R. Yang, *J. Phys. Chem. C* **2011**, *115*, 11302.

[3] a) S. Xu, Y. Wei, M. Kirkham, J. Liu, W. Mai, D. Davidovic, R. L. Snyder, Z. L. Wang, *J. Am. Chem. Soc.* **2008**, *130*, 14958; b) Y. J. Feng, L. L. Liu, X. D. Wang, *J. Mater. Chem.* **2011**, *21*, 15442; c) H. M. Zhang, Y. B. Li, P. R. Liu, Y. Li, D. J. Yang, H. G. Yang, H. J. Zhao, *Chem. Eur. J.* **2012**, *18*, 5165.

[4] a) X. D. Wang, C. J. Summers, Z. L. Wang, *Nano Lett.* **2004**, *4*, 423; b) L. Adler-Abramovich, D. Aronov, P. Beker, M. Yevnin, S. Stempler, L. Buzhansky, G. Rosenman, E. Gazit, *Nat. Nanotechnol.* **2009**, *4*, 849; c) M. Stadermann, S. P. Sherlock, J. B. In, F. Fornasiero, H. G. Park, A. B. Artyukhin, Y. M. Wang, J. J. De Yoreo, C. P. Grigoropoulos, O. Bakajin, A. A. Chernov, A. Noy, *Nano Lett.* **2009**, *9*, 738.

[5] a) P. Poizot, S. Laruelle, S. Grugeon, L. Dupont, J. M. Tarascon, *Nature* **2000**, *407*, 496; b) W. Y. Li, L. N. Xu, J. Chen, *Adv. Funct. Mater.* **2005**, *15*, 851; c) B. Varghese, Y. S. Zhang, L. Dai, V. B. C. Tan, C. T. Lim, C. H. Sow, *Nano Lett.* **2008**, *8*, 3226; e) J. Jiang, J. P. Liu, X. T. Huang, Y. Y. Li, R. M. Ding, X. X. Ji, Y. Y. Hu, Q. B. Chi, Z. H. Zhu, *Cryst. Growth Des.* **2010**, *10*, 70; f) X. H. Xia, J. P. Tu, Y. J. Mai, X. L. Wang, C. D. Gu, X. B. Zhao, *J. Mater. Chem.* **2011**, *21*, 9319.

[6] a) R. Xu, H. C. Zeng, *J. Phys. Chem. B* **2003**, *107*, 926; b) R. Xu, H. C. Zeng, *Langmuir* **2004**, *20*, 9780; c) K. T. Nam, D. W. Kim, P. J. Yoo, C. Y. Chiang, N. Meethong, P. T. Hammond, Y. M. Chiang, A. M. Belcher, *Science* **2006**, *312*, 885; d) Z. Dong, Y. Y. Fu, Q. Han, Y. Y. Xu, H. Zhang, *J. Phys. Chem. C* **2007**, *111*, 18475; e) L. H. Hu, Q. Peng, Y. D. Li, *J. Am. Chem. Soc.* **2008**, *130*, 16136.

[7] a) Y. G. Li, B. Tan, Y. Y. Wu, *J. Am. Chem. Soc.* **2006**, *128*, 14258; b) Y. G. Li, B. Tan, Y. Y. Wu, *Nano Lett.* **2008**, *8*, 265; c) Y. Tak, K. Yong, *J. Phys. Chem. C* **2008**, *122*, 74; d) L. Li, Y. Li, S. Y. Gao, N. Koshizaki, *J. Mater. Chem.* **2009**, *19*, 8366; e) X. Y. Xue, S. Yuan, L. L. Xing, Z. H. Chen, B. He, Y. J. Chen, *Chem. Commun.* **2011**, *47*, 4718; f) X. H. Xia, J. P. Tu, X. L. Wang, C. D. Gu, X. B. Zhao, *Chem. Commun.* **2011**, *47*, 5786; g) X. H. Xia, J. P. Tu, Y. J. Mai, X. L. Wang, C. D. Gu, X. B. Zhao, *J. Mater. Chem.* **2011**, *21*, 9319.

[8] a) M. Mazur, *J. Phys. Chem. C* **2008**, *112*, 13528; b) S. Wolfgang, R. Georg, *Chem. Eng. Sci.* **2006**, *61*, 4973; c) V. Bajpai, P. G. He, L. M. Dai, *Adv. Funct. Mater.* **2004**, *14*, 145; d) L. T. Qu, G. Q. Shi, J. Y. Yuan, G. Y. Han, F. E. Chen, *J. Electroanal. Chem.* **2004**, *561*, 149.

[9] a) G. X. Tong, J. G. Guan, Z. D. Xiao, F. Z. Mou, W. Wang, G. Q. Yan, *Chem. Mater.* **2008**, *20*, 3535; b) G. X. Tong, J. G. Guan, X. A. Fan, W. Wang, F. H. Song, *Chin. J. Inorg. Chem.* **2008**, *24*, 270; c) G. X. Tong, J. G. Guan, Z. D. Xiao X. Huang, Y. Guan, *J. Nanopart. Res.* **2010**, *12*, 3025.

[10] a) J. Estellé, P. Salagre, Y. Cesteros, M. Serra, F. Medina, J. E. Sueiras, *Solid State Ionics* **2003**, *156*, 233; b) P. Erri, P. Pranda, A. Varma, *Ind. Eng. Chem. Res.* **2004**, *43*, 3092; c) N. S. Gajbhiye, S. Prasad, *Thermochimica. Acta* **1996**, *285*, 325; d) P. Pramanik, A. Pathak, *Bull. Mater. Sci.* **1994**, *17*, 967; e) S. Castro, M. Gayoso, C. Rodriguez, *J. Solid State Chem.* **1997**, *134*, 227; f) Z. X. Yue, L. T. Li, J. Zhou, H. G. Zhang, Z. L. Gui, *Mater. Sci. Eng.* **1999**, *B64*, 68; g) S. K. Apte, S. D. Naik, R. S. Sonawane, B. B. Kale, *J. Am. Ceram. Soc.* **2007**, *90*, 412.

[11] a) L. T. Qu, G. Q. Shi, F. E. Chen, J. X. Zhang, *Macromolecules* **2003**, *36*, 1063; b) J. Y. Yuan, L. T. Qu, D. Q. Zhang, G. Q. Shi, *Chem. Commun.* **2004**, *8*, 994.

[12] M. Mazur, A. Michota-Kaminska, J. Bukowska, *J. Electrochem. Commun.* **2007**, *9*, 2418.

[13] M. Mazur, A. Frydrychewicz, *J. Appl. Polym. Sci.* **2007**, *106*, 2169.

[14] L. Guo, F. Liang, X. G. Wen, S. H. Yang, L. He, W. Z. Zheng, C. P. Chen, Q. P. Zhong, *Adv. Funct. Mater.* **2007**, *17*, 425.

[15] S. M. Yoon, H. C. Choi, *Curr. Appl. Phys.* **2006**, *6*, 747.

[16] Ž. D. Živković, D. T. Živković, D. B. Grujičić, *J. Therm. Anal.* **1998**, *53*, 617.

[17] W. M. Keely, H. W. Maynor, *J. Chem. Eng. Data* **1963**, *8*, 297.

[18] a) E. Fouissac, M. Milas, M. Rinaudo, *Macromolecules* **1993**, *26*, 6945; b) J. Kestin, H. E. Khalifa, R. J. Correia, *J. Phys. Chem. Ref. Data* **1981**, *10*, 71.

[19] S. A. Makhlouf, *J. Magn. Magn. Mater.* **2002**, *246*, 184.

[20] Y. G. Zhang, Y. C. Chen, T. Wang, J. H. Zhou, Y. G. Zhao, *Microporous Mesoporous Mater.* **2008**, *114*, 257.

[21] W. L. Roth, *J. Phys. Chem. Solids* **1964**, *25*, 1.

[22] a) T. Ambrose, C. L. Chien, *Phys. Rev. Lett.* **1996**, *76*, 1743; b) Y. Ichiyanagi, S. Yamada, *Polyhedron* **2005**, *24*, 2813; c) P. Dutta, M. S. Seehra, S. Thota, J. Kumar, *J. Phys.: Condens. Matter* **2008**, *20*, 015218.

[23] C. Nethravathi, S. Sen, N. Ravishankar, M. Rajamathi, C. Pietzonka, B. Harbrecht, *J. Phys. Chem. B* **2005**, *109*, 11468.

[24] L. Néel, in Low-Temperature Physics (Eds: C. Dewitt, B. Dreyfus, P. D. de Gennes), Gordan and Breach, New York **1997**, p. 413.

[25] R. H. Kodama, S. A. Makhlouf, A. E. Berkowitz, *Phys. Rev. Lett.* **1997**, *79*, 1393.

[26] a) M. Verelst, T. Ould-Ely, C. Amiens, E. Snoeck, P. Lecante, A. Mosset, M. Respaud, J. M. Broto, B. Chaudret, *Chem. Mater.* **1999**, *11*, 2702; b) R. M. Wang, C. M. Liu, H. Z. Zhang, C. P. Chen, L. Guo, H. B. Xu, S. H. Yang, *Appl. Phys. Lett.* **2004**, *85*, 2080; c) M. Kiwi, *J. Magn. Magn. Mater.* **2001**, *234*, 584.

[27] E. L. Salabas, A. Rumplecker, F. Kleitz, F. Radu, F. Schüth, *Nano Lett.* **2006**, *6*, 2977.

[28] X. P. Shen, H. J. Miao, H. Zhao, Z. Xu, *Appl. Phys. A* **2008**, *91*, 47.

[29] a) G. X. Tong, J. H. Yuan, J. Ma, J. G. Guan, W. H. Wu, L. C. Li, R. Qiao, *Mater. Chem. Phys.* **2011**, *129*, 1189; b) G. X. Tong, W. H. Wu, R. Qiao, J. H. Yuan, J. G. Guan, H. S. Qian, *J. Mater. Res.* **2011**, *26*, 1639; c) G. X. Tong, W. H. Wu, J. G. Guan, J. P. Wang, J. Ma, J. H. Yuan, S. L. Wang, *J. Mater. Res.* **2011**, *26*, 2590;

d) J. H. He, W. Wang, J. G. Guan, *J. Appl. Phys.* **2012**, *111*, 093924.

[30] a) D. Larcher, G. Sudant, J. B. Leriche, Y. Chabre, J. M. Tarascon, *J. Electrochem. Soc.* **2002**, *149*, A234; b) N. Du, H. Zhang, B. D. Chen, J. B. Wu, X. Y. Ma, Z. H. Liu, Y. Q. Zhang, D. R. Yang, X. H. Huang, J. P. Tu, *Adv. Mater.* **2007**, *19*, 4505.

[31] S. Grugeon, S. Laruelle, R. Herrera-Urbina, L. Dupont, P. Poizot, J. M. Tarascon, *J. Electrochem. Soc.* **2001**, *148*, A285.

[32] L. Tian, H. L. Zou, J. X. Fu, X. F. Yang, Y. Wang, H. L. Guo, X. H. Fu, C. L. Liang, M. M. Wu, P. K. Shen, Q. M. Gao, *Adv. Funct. Mater.* **2010**, *20*, 617.

[33] I. A. Courtney, W. R. McKinnon, J. R. Dahn, *J. Electrochem. Soc.* **1999**, *146*, 59.

[34] S. Denis, E. Baudrin, M. Touboul, J. M. Tarascon, *J. Electrochem. Soc.* **1997**, *144*, 4099.

[35] G. Binotto, D. Larcher, A. S. Prakash, R. Herrera Urbina, M. S. Hegde, J. M. Rarascon, *Chem. Mater.* **2007**, *19*, 3032.

[36] B. Guo, C. S. Li, Z. Y. Yuan, *J. Phys. Chem. C* **2010**, *114*, 12805.

[37] a) M. S. Park, G. X. Wang, Y. M. Kang, D. Wexler, S. X. Dou, H. K. Liu, *Angew. Chem. Int. Ed.* **2007**, *46*, 750; b) Y. Wang, H. C. Zeng, J. Y. Lee, *Adv. Mater.* **2006**, *18*, 645.